RESEARCH ARTICLE

Macromolecular Bioscience

www.mbs-journal.de

# Design of Suspended Melt Electrowritten Fiber Arrays for Schwann Cell Migration and Neurite Outgrowth

*Andrei Hrynevich, Pascal Achenbach, Tomasz Jungst, Gary A. Brook,* and Paul D. Dalton**

**In this study, well-defined, 3D arrays of air-suspended melt electrowritten fibers are made from medical grade poly(ε-caprolactone) (PCL). Low processing temperatures, lower voltages, lower ambient temperature, increased collector distance, and high collector speeds all aid to direct-write suspended fibers that can span gaps of several millimeters between support structures. Such processing parameters are quantitatively determined using a "wedge-design" melt electrowritten test frame to identify the conditions that increase the suspension probability of long-distance fibers. All the measured parameters impact the probability that a fiber is suspended over multimillimeter distances. The height of the suspended fibers can be controlled by a concurrently fabricated fiber wall and the 3D suspended PCL fiber arrays investigated with early post-natal mouse dorsal root ganglion explants. The resulting Schwann cell and neurite outgrowth extends substantial distances by 21 d, following the orientation of the suspended fibers and the supporting walls, often generating circular whorls of high density Schwann cells between the suspended fibers. This research provides a design perspective and the fundamental parametric basis for suspending individual melt electrowritten fibers into a form that facilitates cell culture.**

## 1. Introduction

Melt electrowriting (MEW) uses an electrohydrodynamic phenomenon that sustains a fluid column without Plateau-Raleigh instabilities at low flow rates,[1,2] resulting in fibers as small as 820 nm in diameter.[3] With MEW, the nozzle is raised above a moving collector as a thin molten fluid column, or jet, rapidly cools on the collector into a defined fiber. When layered repeatedly[4] a highly porous scaffold can be fabricated that is readily penetrated by cells and therefore has utility in biomedical applications. Detailed reviews on the MEW technology can be found elsewhere.[5,6]

To date, MEW scaffolds have been primarily made with a "box-pore" morphology, due to simple programming. On closer inspection for certain scaffold morphologies, there are several instances where suspended fibers spontaneously occur within these scaffolds. For instance, when small pores are targeted,[7] less repeated printing paths are used,[8] or higher-order printing pathways are developed (i.e., octagonal or dodecagonal patterns)[9] the phenomenon of suspended fibers can be seen within scaffolds. Such suspended fibers over such small lengths have also been described as "jumping" or "bridging" fibers and are considered a defect in the pursuit of well-formed scaffolds.[5]

Suspended fibers, i.e., those that span across an air gap, have also long been observed in solution electrospinning,[10] and some studies used this phenomenon to transfer orientated fibers to other substrates for guided cell growth studies.[11] Due to the nature of electrical instabilities in solution electrospinning,[12]

A. Hrynevich, Dr. T. Jungst, Prof. P. D. Dalton
Department of Functional Materials in Medicine and Dentistry and Bavarian Polymer Institute
Julius Maximilians University of Würzburg
Pleicherwall 2, Würzburg 97070, Germany
E-mail: paul.dalton@fmz.uni-wuerzburg.de; daltonlab@gmail.com

The ORCID identification number(s) for the author(s) of this article can be found under https://doi.org/10.1002/mabi.202000439



**DOI: 10.1002/mabi.202000439**

A. Hrynevich
Department of Veterinary Science
Utrecht University
Yalelaan 1 Utrecht 3584 CL , Netherlands

A. Hrynevich
Department of Orthopedics
UMC Utrecht
Heidelberglaan 100 Utrecht 3584 CX, Netherlands

P. Achenbach, Dr. G. A. Brook
Institute of Neuropathology
RWTH Aachen University Hospital
Pauwelsstrasse 30 Aachen 52074, Germany
E-mail: gbrook@ukaachen.de

Prof. P. D. Dalton
Phil and Penny Knight Campus for Accelerating Scientific Impact
University of Oregon
1505 Franklin Boulevard Eugene 97403-6231, USA

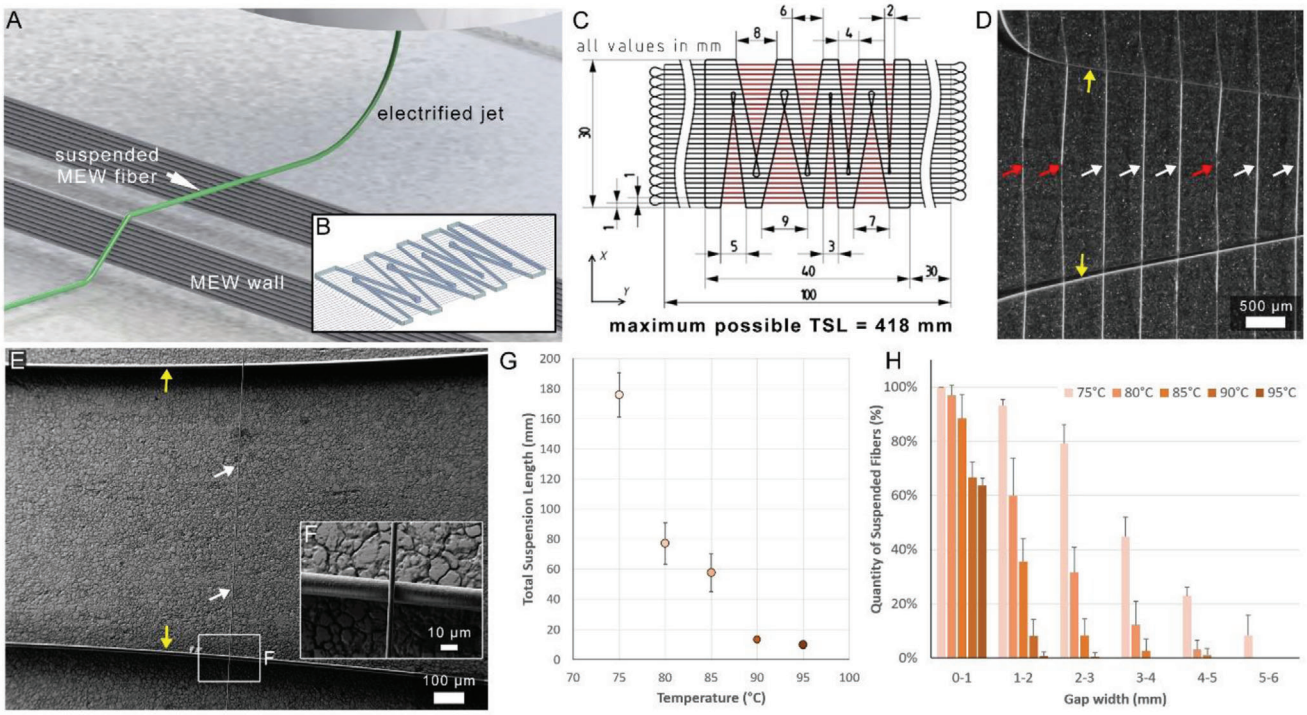


**Figure 1.** Establishment of the suspended fiber test frame. A) Rendering of the MEW jet that is direct-written across concurrently fabricated walls to create suspended fibers. B) Inset showing the rendering of the suspended fiber test frame that is shown from above in (C), where a spectrum of different spanning gaps is provided, shown in the area marked red. A maximum total fiber suspension length (TSL) of 418 mm is possible. D) Photograph showing how the suspended fibers are visually checked on the stereomicroscope, to calculate the TSL. White and red arrows indicate fibers that succeed and fail to suspend across the gap, respectively. Yellow arrows indicate the MEW-fiber wall that is used to create the spanning gap. E) SEM image of a suspended fiber (white arrows) between a gap while the inset (F) shows a magnified image of the fiber/wall crossover point. G) A graph showing the TSL as a function of set temperature for the polymer while (H) is a further breakdown of the various spanning gaps that each condition in (G) was able to achieve.

however, such fibers are difficult to directly place in discrete locations without them crossing over each other. Recently, different parametric conditions such as low-voltage direct writing with polymer solutions have been used to discretely place fibers that span gaps for pressure sensor applications.[13] There are other instances with metallic colloids and melts in which direct-writing can span large air gaps[14] where the rapid solidification of an ink allows self-supporting structures to be made. Suspended fibers (**Figure 1**A) are therefore an interesting design capability for MEW, that has not yet been fully investigated. The 3D control of the pattern of populations of suspended, orientated fibers opens potential future applications in the reconstruction of highly organized, anisotropic structures after traumatic injury, such as nerves of the peripheral nervous system (PNS). A pilot investigation of the ability of the MEW generated scaffold to influence neural cell migration and neurite outgrowth was therefore performed using early post-natal mouse dorsal root ganglia (DRG) explants.

### 1.1. Effect of Polymer Melt Temperature on Fiber Suspension

PCL was measured to have a melting point of 58.4 °C (Figure S1, Supporting Information). A test frame (Figure 1B,C) consisting of MEW fiber walls was designed so that a spectrum of different gaps for suspended fibers could be tested under different processing conditions. Through visual inspection of each region (Figure 1D), either successful (white arrow) or failed (red arrow) suspension between fiber walls (yellow arrow) was determined, with a challenging cumulative maximum possible total suspension length (TSL) of 418 mm. The TSL was calculated as a sum of all suspended fiber segments within the wedges (marked red, Figure 1C). Figure 1E shows a scanning electron microscope (SEM) image of a successfully suspended fiber, with Figure 1F showing a magnified image where the suspended fiber and wall intersect.

The polymer melt temperature was found to greatly influence the ability to suspend fibers between the supporting walls (Figure 1G). At temperatures greater than 90 °C almost no suspended fibers are found on a test sample, and the lowest heating temperature of 75 °C resulted in a cumulative total of 176 ± 14 mm (Figure 1G; blue arrow) of suspended fibers out of a possible 418 mm TSL. Figure 1H depicts this effect based on the various spanning gaps and since fiber spanning is a measure of polymer solidification rate, it is expected that the lowest polymer temperatures would improve fiber suspension. The flow rate to the nozzle also increases with the polymer temperature, due to the lower melt viscosity.

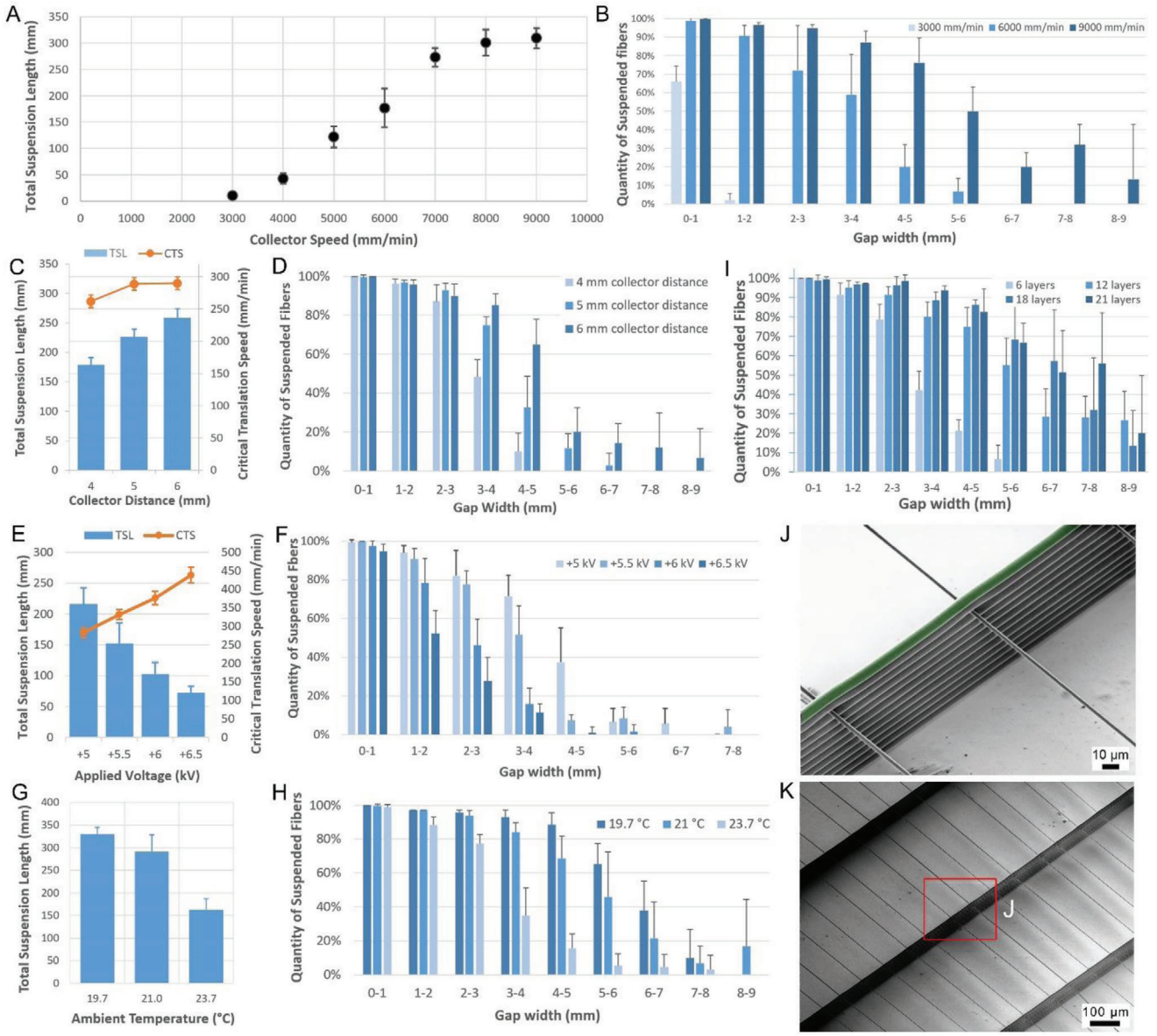


**Figure 2.** Quantitative outcomes of various fibers suspended under different conditions. A) Graph showing the effect of collector speed on the total suspension length (TSL) with further breakdown of each gap shown in (B). C) Graph showing the effect of collector distance on the TSL and critical translation speed (CTS) with further breakdown of each gap shown in (D). E) Graph showing the effect of applied voltage on the TSL with further breakdown of each gap shown in (F). G) Graph showing the effect of ambient temperature on the TSL with further breakdown of each gap shown in (H). I) Graph of the effect of MEW wall fiber height on the fiber suspension probability. J) SEM image how the top fiber (false-colored green) fixes the suspended fiber into position while (K) shows a wider view of suspended fibers.

### 1.2. Effect of Collector Speed on Fiber Suspension

As can be seen in **Figure 2**A,B, the collector speed has an important influence on the ability to suspend fibers. When the collector moved at speeds slower than 3000 mm min$^{-1}$, only occasional suspended fibers were observed, whereas at 6000 mm min$^{-1}$ fibers on the shorter distances of the test frame were suspended. The fiber suspension probability across a larger spanned gap, however, was greatest at 9000 mm min$^{-1}$. As previously reported, faster collector speeds result in more elongated MEW jets[15] and these would be expected to cool more rapidly, contributing to more suspended fiber generation.

In this study, the collector speed is the only variable which does not have a direct influence on jet stability[15] and is limited by the maximal stage speed and acceleration which has a strong effect on fiber diameter. As previously reported,[16] the original diameter of the fiber $d$ after switching from speed $S_1$ to $S_2$ changes to $D = d\sqrt{S_1/S_2}$. Under the current conditions, this corresponds to a fiber diameter of ≈2–3 µm for the suspended fiber. If a specific fiber thickness is required, pressure adjustment (along with

other parameters) could become necessary, which will in its turn also affect the ability to generate suspended fibers. Further information on the impact of applied pressure is provided in the Figures S2 and S3 in the Supporting Information.

### 1.3. Effect of Collector Distance and Voltage on Fiber Suspension

Similar to how the jet cooling rate affected previous parameters, increasing the collector distance improved the fiber suspension (Figure 2C,D). Here, two variables are altered: the reduced electrostatic forces (correlated in Figure 2E) and a longer jet path that allows more cooling. Nevertheless, the application of an increased collector distance for suspended fiber printing should be considered with caution. Due to the preferred lower electric fields for fiber suspension, a dynamic voltage approach[4] is required to maintain the electrical field without fiber pulsing.

With a decreasing applied voltage, forces acting on the charged polymer in the jet are expected to decrease. Consequently, the jet speed, estimated by the critical translation speed (CTS),[17] decreases and the TSL increases significantly with each 0.5 kV reduction of the applied voltage (Figure 2E,F). In this context, the jet lag would also increase[18] and similarly lead to more cooling of the jet before deposition on the collector. For both collector distance and applied voltage adjustment, there are limits due to the result of fiber pulsing, a MEW-specific manufacturing defect that can predominate at lower electric fields.[15]

### 1.4. Effect of Ambient Temperature on Fiber Suspension

While the printers used here do not have climate control, measurements were performed based on three different laboratory temperatures. Relatively small changes in the ambient air temperature had a substantial impact on fiber suspension: only a 4 °C increase (from 19.7 to 23.7 °C) resulted in a 50% reduction in the TSL (Figure 2G,H). Therefore, improved control of the ambient environment is required for more reliable experimental results and lower temperatures provide a potential opportunity to improve fiber suspension. While humidity was kept within a certain range (25–40% r.h.), a previous study shows that such small differences at room temperature do not have a substantial impact on MEW.[19]

### 1.5. Effect of Wall Height on Fiber Suspension

The height of the MEW fiber wall affects the probability of fiber suspension, which correlates with out-of-plane experiments previously reported.[20] Since the test frame is designed to aggregate a specific measure (i.e., whether a spanning fiber is fully suspended or not), a lower profile fiber wall from which to perform suspension is expected to reduce that probability (Figure 2I). It was found that six-layer walls (corresponding to ≈80 µm height) could reliably suspend fibers only below gap widths of 1 mm, which should be taken into account for the following suspended fiber array designs.

Test frames also required immediate measuring after printing, as mechanical relaxation of the suspended fibers can occur (Figure S4, Supporting Information). Using optimized conditions investigated here, coupled with the addition of a supplementary MEW fiber to anchor the wall (Figure 2J), the production of well-suspended fiber arrays could be achieved (Figure 2K).

### 1.6. Controlling the Height and Position of Suspended Fibers

Based on the limits and parameters that affect the suspension of fibers using the test frame, more complex designs can be developed. To generate a true 3D orientated fiber construct, the number of fibers within the wall could be used to control the fiber suspension height. **Figure 3**A shows a SEM image of a suspended fiber array where one fiber is placed directly above another, at either 80 and 240 µm or 160 and 320 µm above the collector. The suspended fibers are "embedded" in the fiber wall with the additional layers, including the top suspended fiber that is fixed in position with a final MEW fiber (false-colored green).

Suspended fibers could also be direct-written at an angle with respect to the fiber wall. Figure 3B shows how 16 suspended fibers intersect the wall at 45°, four fibers (≈50 µm) above each other with minimal defects. Notably, it is the control of the fiber position in the X–Y plane that is the most inaccurate, highlighted in Figure 3C with a red dotted line approximating the *z*-axis and slight offsets at the suspended fiber/wall intersection point. Furthermore, the intersection of the suspended fibers also has slight X–Y plane offsets, shown in Figure 3D–F. This variance is likely due to errors caused by electrostatic interactions,[21] or acceleration of the jet from a nonideal location at the turning point.[15]

A "step-ladder" design approach for aligned suspended fibers was used for in vitro experiments, so that both the Z-position and the lateral position were shifted for each suspended fiber, shown in Figure 3G and highlighted in Figure 3H. When these fiber arrays are fabricated without an external structural support, however, they contract and the resolution and positioning of the suspended fibers is lost (Figure 3I and Figure S5, Supporting Information). To improve the design for handling such scaffolds during frequent media changes, fixation and immunocytochemical staining, an additional external ring was also incorporated. This third component (after the fiber wall and suspended fibers) of the suspended fiber arrays is also made using MEW, but with a direct writing speed below the CTS. This reinforced the entire construct, and the final design for cell culture is schematically represented in **Figure 4**A, with step-ladder suspended fibers shown in Figure 4B,C.

### 1.7. Schwann Cell Migration from Explanted Dorsal Root Ganglia

Immediately after positioning on to the MEW scaffolds, the DRG showed a clear rounded appearance (data not shown). Samples processed for S100 peroxidase immunocytochemistry after 21 days in vitro (DIV) demonstrated the resulting pattern of the DRG explant-derived Schwann cell spreading. Large sheets of cells could be seen extending or migrating across the scaffold following the trajectory of the supporting walls for several millimeters (Figure 4D,E; white arrows) as well as that of the suspended fibers for distances of ≈1 mm (Figure 4D; black arrows). The cell–cell adhesion between Schwann cells migrating along the suspended PCL fibers, as well as along the supporting walls, resulted in the appearance of whorls of migrating cells, forming

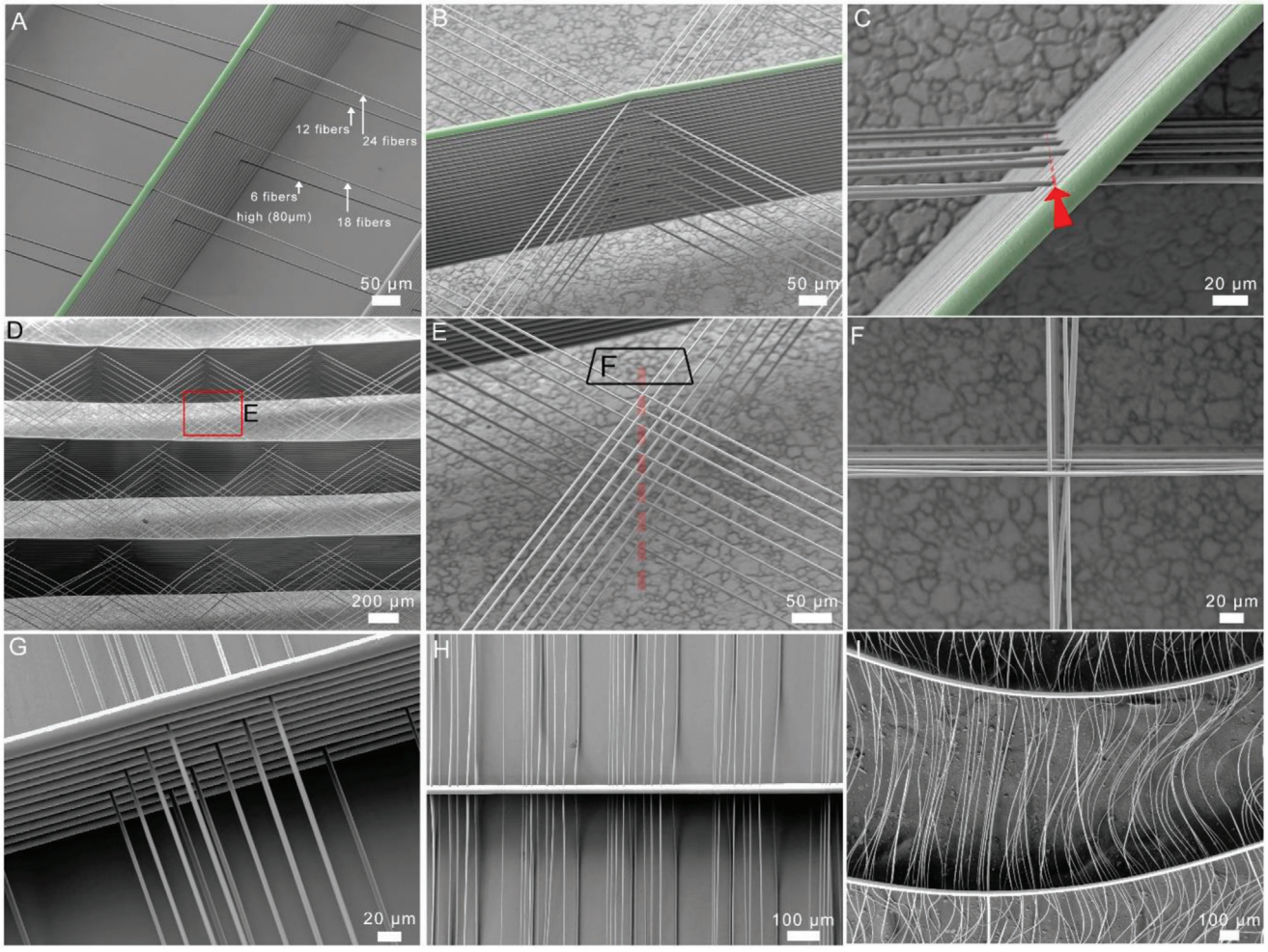


**Figure 3.** SEM images of suspended fibers. A) showing how the *z*-axis position of the suspended fiber can be controlled through the wall height (6, 12, 18, and 24 fiber layers corresponding to 80, 160, 240, and 320 μm respectively), while an additional MEW fiber on the wall (false-colored green) locks the upper suspended fiber into place. B) Suspended fibers intersecting the fiber wall at 45°. C) Top view of suspended fiber and wall intersection points, showing small X–Y positioning errors occur (*z*-axis approximately indicated with red dashed line). D) A suspended fiber array with 16 fiber crossover points, shown in E) magnification of the suspended fiber crossover and F) from above. G) Example of the "step-ladder" fiber design developed for the in vitro research, also shown in(H) from above. (I) shows how without an additional mechanical support (implemented by printing a ring support), such suspended fiber arrays can collapse and lose their structure.

ovoid-shaped holes or pores (Figure 4E; asterisks). Higher magnification demonstrated the bipolar, spindle-shaped morphology of individual migrating Schwann cells that followed the orientation dictated by their adhesion to the suspended PCL fibers, or even as they spanned gaps of 200 μm or more between the adjacent arrays of fibers (Figure 4F; white arrow).

### 1.8. Neurite Outgrowth from Explanted Dorsal Root Ganglia

Samples processed for combined NF200 and ß III-tubulin immunocytochemistry after 21 DIV demonstrated the growth pattern of the DRG-derived neurites. The intensely stained neurites extended as small fascicles or individual fibers from the neurons clustered within the ganglion. Similar to the migratory behavior of the Schwann cells, the DRG-derived neurites adopted trajectories that followed the orientation of the supporting walls (Figure 4G,H; white arrows) as well as that of the suspended fibers (Figure 4I,J; black arrows). The neurites growing in close association with suspended fibers displayed simple growth cone-like tips (Figure 4J; black arrows). Although many neurites that grew across the gaps between adjacent suspended fibers adopted the orientation of those fibers once contact had been established, surprisingly many others appeared to by-pass completely the suspended fibers and continue their direction of growth that was largely orthogonal to that of the suspended fibers (Figure 4I; black arrows). This pattern of neurite extension appeared to readily bridge the gaps or pores between adjacent fibers.

The interconnectivity of the scaffold supported the attachment and migration of cells, the extension of processes and nutrient/waste exchange. The finely engineered topographical features (e.g., the surface curvature and alignment of micro- and nanofibers) are known features of neural tissue engineering scaffolds that exert profound effects on adherent cell form and

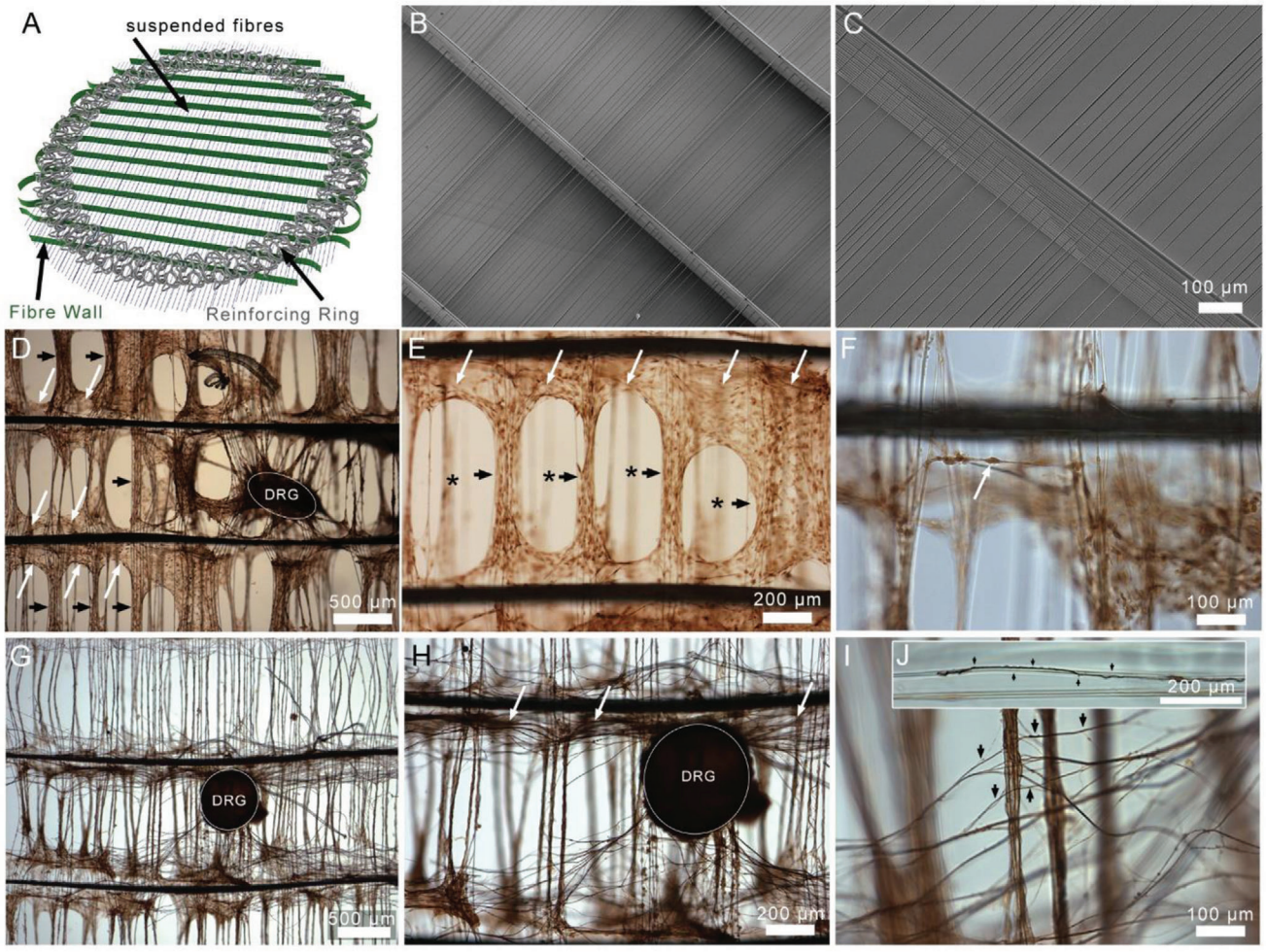


**Figure 4.** Suspended fiber arrays after 21 DIV with dorsal root ganglion (DRG) explants. A) Rendering of the reinforced suspended array frame and B) SEM image of the extended "step-ladder" design previously shown in Figure 3G and H) at higher magnification. D–F) Low and mid-power magnification of S100-immunoreactive Schwann cell migration that results in the formation of sheets of cells that follow the trajectory of the supporting walls (white arrows) as well as that of the suspended fibers (black arrows) of the scaffold. The profile of the explanted DRG is indicated by the white circle. F) A single spindle-shaped, bipolar Schwann cell with a small ovoid cell body can be seen spanning gaps (e.g., 200 µm) between suspended PCL fibers (white arrow). G–J) Low power microscopy of the florid pattern of ß-III tubulin/NF200-positive neurite extension from an explanted DRG. Multiple small fascicles of neurites (white arrows) can be seen following the general orientation of the supporting walls and by-passing many of the orthogonally positioned suspended fibers. I) Many loosely scattered neurites (black arrows) can be seen by-passing the suspended fibers. J) Individual neurite (black arrows) closely following the orientation of a single, suspended fiber with an approximate diameter of 3 µm.

function including process extension and cell migration.[11,22–26] Earlier in vitro studies in which multiple arrays of orientated electrospun PCL nanofibers were suspended in a 3D fibrin hydrogel revealed a tendency for embedded Schwann cells to align along the topographical cues provided by the non-functionalized fibers rather than migrating through the fibrin hydrogel.[27] Fabrication of hollow nerve guides containing orientated PCL nanofibers in a gelatin hydrogel intraluminal filler was used to investigate functional tissue repair following 15 mm resection injuries of the adult rat sciatic nerve. Although the fiber/hydrogel-containing implant promoted better anatomical and functional tissue repair than empty conduits, the 3D pattern of orientated nanofibers was somewhat unstable within the gelatin hydrogel and the performance of the implant was still inferior to that of the autograft.[28] Other recent developments in PNS tissue engineering and regenerative medicine have also focused on the generation of scaffolds that reproduce essential aspects of physical/structural guidance cues within implantable hollow conduits.[29,30] The present study describes the control of key parameters that are required for MEW fabrication of robust 3D scaffolds with suspended, orientated fibers of well-defined spacing, as well and a preliminary indication of how DRG neurons and Schwann cells respond to such scaffolds. A number of research groups have been investigating suspended fiber arrays using solution jet writing, with suspended fibers between the pillars of 3D electrodes.[31,32] Solution-based jetting techniques have traditionally proved challenging for the control of fiber placement and rapid solidification through solvent evaporation. However, such arrays were fabricated with variable spacing between fibers and some degree of over-lapping of fibers.[33,34]

The whorls of Schwann cells seen in this study support observations in other MEW studies and have even been mathematically modeled.[35] Previous scaffolds supported human bone marrow-derived mesenchymal stem cell (BMSC) adhesion and cell whorls formed that outlined the 250 µm pores of the scaffold. Such circular patterns of growth were subsequently confirmed by Xie and colleagues who, using scaffolds with finely controlled fiber diameters, reported circular patterns of BMSC growth within pores surrounded by thick X–Y fibers, a random pattern of growth throughout pores surrounded by thin X-Y fibers, and an orientated pattern of growth within pores surrounded by thick (X) and thin (Y) fibers. Furthermore, cell proliferation was reported to be greater in small pores than in large pores.[36] Other studies on similar scaffolds have also revealed that cell alignment occurs preferentially along the long axis of oblong shaped pores,[37] and that pore size and suspended fiber sagging influence cell growth.[38]

In the present study, 3D suspended fiber scaffolds were shown to support the growth and migration S100-positive Schwann cells from DRG explants over substantial distances, this growth following the orientation of the suspended fibers as well as that of the perpendicularly positioned supporting walls. The resulting pattern of growth generated whorls of cells that strongly resembled that of BMSC cell suspensions seeded onto suspended PCL fibers.[36] The accompanying pattern of ß-III tubulin/NF200-positive neurite outgrowth from the DRG explants was, to some extent, similar in that substantial growth of neurites could be seen extending from the explant and following the general direction dictated by the orientation of the supporting walls. The patterns of neurite outgrowth in these regions was most likely influenced by the large numbers of Schwann cells occupying this position and trajectory. Here, the neurites could be seen either completely by-passing the near-by suspended fibers or modifying their direction to adopt that of the suspended fibers. This pattern of neurite outgrowth supports the well-established influence of Schwann cell surface and extracellular matrix proteins on the direction of neurite outgrowth.[39]

In conclusion, this study used a test frame to identify the ideal parametric conditions for suspending PCL fibers using MEW. Low melt temperatures, high collector speeds, lower voltages, and cooler ambient temperatures all aided in the generation of well-suspended fibers spanning across multi-millimeter distances. The z-position of the fibers was controlled by a simultaneous printing of the suspended fibers and supporting wall. A surrounding ring mechanically supported the frames so that they could withstand repeated media and fluid changes for cell culture as well as the subsequent processing for peroxidase immunocytochemistry. The placing of DRG onto the suspended arrays and the subsequent Schwann cell migration and neurite outgrowth could be readily visualized by simple light microscopy.

## 2. Experimental Section

*Materials*: PCL was sourced from Corbion Inc. (Gorinchem, Netherlands, PURASORB PC 12, Lot# 1412000249, 03/2015) and used as received.

*MEW Printer*: Suspended fibers were manufactured on a custom-built MEW device, described in detail elsewhere[15] and in the Supporting Information. Briefly, a 22-gauge nozzle was screwed into a 3 mL syringe and the polymer temperature/pressure inside the syringe was digitally regulated by two separate heating elements and an air pressure system. The nozzle protruded for ≈0.5 mm out from the head, and the collector was a stainless-steel sheet. The heating temperature indicated, if not specified otherwise, is the one set by the controller, and differs from the actual temperature of the melt exiting the nozzle, discussed further in the Supporting Information.

*Test Frame Suspended Fiber Collection*: A test frame for the investigation of parameters for suspended fibers is shown in Figure 1C and was entirely printed via MEW. The frame contains eight "wedges" with base lengths ranging from 2–9 mm in 1 mm increments. The frame height was achieved by stacking the same pattern six times. In order to minimize its variation, unified process parameters during frame printing were used. Therefore, the frame printing speed had to be slightly adjusted to maintain the same fiber diameter between different prints, to achieve a constant frame height. For the frame walls, an average fiber diameter of 13.6 µm was targeted and standard parameters include $T_p = 75$ °C, $S = 800$ mm min$^{-1}$, $G = 6$ mm, − 1.5 kV collector voltage, and +5 kV nozzle voltage. Under that conditions wall height was ≈82 µm for the six-fiber wall. A total of 30 fibers were direct-written over the gaps provided by the frame. During a single print, three frames with suspended fibers were printed sequentially, with a CTS check in between for process stability validation.

*Suspended Fiber Length Calculation*: Using a stereomicroscope (Discovery V20, Carl Zeiss Microscopy GmbH, Germany), the total length of suspended fiber over the sample was measured. The regions marked red in the Figure 1C where the fibers that did not touch the collector surface were cumulated. Further details on the suspended fiber length calculation can be found in the Supporting Information.

*Fiber Diameter Measurement*: The diameters of suspended fibers were measured with a scanning electron microscope (Zeiss CB 340, Carl Zeiss Microscopy GmbH, Göttingen, Germany). Ten fiber diameters were measured per sample, with five measurement points for each fiber.

*CTS Measurement*: For the CTS measurement parallel arrays of fibers were printed with the collector speed increasing by 10 mm min$^{-1}$ every second line. Minimal speed, at which both fibers were straight was considered as CTS.

*Neural Cell-Substrate Interactions Using Explanted Dorsal Root Ganglia*: All experimental procedures were in accordance with legal regulations discussed further in the Supporting Information. DRG were removed from 12 C57BL/6N mouse pups (postnatal day 5–7, Charles River Laboratories, Sulzfeld, Germany) and placed into sterile, cooled (4 °C) Hanks balanced salt solution (HBSS, Life Technologies, Germany) containing 6.2 mg mL$^{-1}$ glucose.

Scaffolds were sterilized (70% ethanol, 30 min) followed by 2 × 5 min washes in HBSS and precoated with poly-L-lysine (PLL, Merck, Germany, 100 µg mL$^{-1}$ in sterile MilliQ water, 30 min), washed again in sterile MilliQ water, and finally incubated in laminin (Merck, 10 µg mL$^{-1}$ in HBSS, 1 h). The PLL/laminin coated PCL scaffolds were then placed into 24-well tissue culture plates containing Dulbecco's Modified Eagle's Medium with Glutamax (1:100), 10% fetal calf serum and antibiotic/antimycotic solution (penicillin/streptomycin/fungizone, diluted 1:100, Thermofischer, Germany). DRG explants were then carefully placed onto the scaffold and placed into a humidified incubator (37 °C, 5% $CO_2$) for 3 h to allow adhesion. A sterile plastic ring held the scaffold in place and an extra volume of 1.0 mL medium added. After 21 DIV, samples were washed for 2 × 5 min in HBSS, then fixed by immersion in cold 4% paraformaldehyde (AppliChem, Germany) for 30 min.

*Immunocytochemistry*: After fixation, samples underwent immunocytochemistry as described in detail in the Supporting Information. DRG explant-derived Schwann cells were identified using polyclonal anti-S100ß (1:2000, DAKO Products, Germany), and explant-derived neurites were identified with a combination of monoclonal antibodies: mouse anti-phosphorylated neurofilament 200 kDa (1:2000, Sigma-Aldrich) and mouse anti-ß III tubulin (1:1000, Sigma-Aldrich, Germany). Samples were visualized by placing them in a custom-made well filled with an 8:1 glycerol/phosphate-buffered saline mixture and topped with a coverslip. Images were taken using a Zeiss Axioplan microscope coupled to a digital camera (Zeiss Axiocam) and Axiovision software.

## Supporting Information

Supporting Information is available from the Wiley Online Library or from the author.

## Acknowledgements

The technical assistance of Dr. Claus Moseke and Judith Friedlein for SEM imaging, and Almoatazbellah Youssef for the MEW ring design development is appreciated. Financial assistance from the Volkswagen Foundation (grant 93417) is acknowledged while the German Research Foundation (DFG) State Major Instrumentation Programme (INST 105022/58-1 FUGG) funded the Zeiss Crossbeam CB 340 SEM used in this study.

Open access funding enabled and organized by Projekt DEAL.

## Conflict of Interest

The authors declare no conflict of interest.

## Data Availability Statement

Data available on request from the authors.

## Keywords

cell migration, electrospinning, fibers, neurite growth, polycaprolactone, tissue engineering

Received: February 19, 2021
Published online: May 5, 2021

[1] Á. G. Marín, D. Lohse, *Phys. Fluids* **2010**, *22*, 122104.
[2] P. D. Dalton, *Curr. Opin. Biomed. Eng.* **2017**, *2*, 49.
[3] G. Hochleitner, T. Jungst, T. D. Brown, K. Hahn, C. Moseke, F. Jakob, P. D. Dalton, J. Groll, *Biofabrication* **2015**, *7*, 035002.
[4] F. M. Wunner, M. L. Wille, T. G. Noonan, O. Bas, P. D. Dalton, E. M. De-Juan-Pardo, D. W. Hutmacher, *Adv. Mater.* **2018**, *30*, 1706570.
[5] T. M. Robinson, D. W. Hutmacher, P. D. Dalton, *Adv. Funct. Mater.* **2019**, *29*, 1904664.
[6] J. C. Kade, P. D. Dalton, *Adv. Healthcare Mater.* **2020**, *n/a*, 2001232.
[7] T. Tylek, C. Blum, A. Hrynevich, K. Schlegelmilch, T. Schilling, P. D. Dalton, J. Groll, *Biofabrication* **2020**, *12*, 025007.
[8] T. D. Brown, P. D. Dalton, D. W. Hutmacher, *Adv. Mater.* **2011**, *23*, 5651.
[9] A. Youssef, A. Hrynevich, L. Fladeland, A. Balles, J. Groll, P. D. Dalton, S. Zabler, *Tissue Eng., Part C* **2019**, *25*, 367.
[10] P. D. Dalton, D. Klee, M. Moller, *Polymer* **2005**, *46*, 611.
[11] E. Schnell, K. Klinkhammer, S. Balzer, G. Brook, D. Klee, P. Dalton, J. Mey, *Biomaterials* **2007**, *28*, 3012.
[12] D. H. Reneker, A. L. Yarin, *Polymer* **2008**, *49*, 2387.
[13] W. Wang, K. Ouaras, A. L. Rutz, X. Li, M. Gerigk, T. E. Naegele, G. G. Malliaras, Y. Y. S. Huang, *Sci. Adv.* **2020**, *6*, eaba0931.
[14] M. A. Skylar-Scott, S. Gunasekaran, J. A. Lewis, *Proc. Natl. Acad. Sci. U. S. A.* **2016**, *113*, 6137.
[15] G. Hochleitner, A. Youssef, A. Hrynevich, J. N. Haigh, T. Jungst, J. Groll, P. D. Dalton, *BioNanomaterials* **2016**, *17*, 159.
[16] A. Hrynevich, B. S. Elci, J. N. Haigh, R. McMaster, A. Youssef, C. Blum, T. Blunk, G. Hochleitner, J. Groll, P. D. Dalton, *Small* **2018**, *14*, 1800232.
[17] G. Hochleitner, E. Fursattel, R. Giesa, J. Groll, H. W. Schmidt, P. D. Dalton, *Macromol. Rapid Commun.* **2018**, *39*, 1800055.
[18] A. Hrynevich, I. Liashenko, P. D. Dalton, *Adv. Mater. Technol.* **2020**, *5*, 2000772.
[19] S. Liao, B. Langfield, N. Ristovski, C. Theodoropoulos, J. Hardt, K. A. Blackwood, S. D. Yambem, S. D. Gregory, M. A. Woodruff, S. Powell, *BioNanomaterials* **2016**, *17*, 173.
[20] M. de Ruijter, A. Hrynevich, J. N. Haigh, G. Hochleitner, M. Castilho, J. Groll, J. Malda, P. D. Dalton, *Small* **2018**, *14*, 1702773.
[21] H. Ding, K. Cao, F. Zhang, W. Boettcher, R. C. Chang, *Mater. Des.* **2019**, *178*, 107857.
[22] R. M. Smeal, R. Rabbitt, R. Biran, P. A. Tresco, *Ann. Biomed. Eng.* **2005**, *33*, 376.
[23] R. M. Smeal, P. A. Tresco, *Exp. Neurol.* **2008**, *213*, 281.
[24] B. Schlosshauer, L. Dreesmann, H. E. Schaller, N. Sinis, *Neurosurgery* **2006**, *59*, 740.
[25] C. S. Chen, M. Mrksich, S. Huang, G. M. Whitesides, D. E. Ingber, *Science* **1997**, *276*, 1425.
[26] C. S. Chen, M. Mrksich, S. Huang, G. M. Whitesides, D. E. Ingber, *Biotechnol. Prog.* **1998**, *14*, 356.
[27] D. Hodde, J. Gerardo-Nava, V. Wöhlk, S. Weinandy, S. Jockenhövel, A. Kriebel, H. Altinova, H. W. M. Steinbusch, M. Möller, J. Weis, J. Mey, G. A. Brook, *Eur. J. Neurosci.* **2016**, *43*, 376.
[28] A. Kriebel, M. Rumman, M. Scheld, D. Hodde, G. Brook, J. Mey, *J. Biomed. Mater. Res., Part B* **2014**, *102*, 356.
[29] P. A. Wieringa, A. R. Gonçalves de Pinho, S. Micera, R. J. A. van Wezel, L. Moroni, *Adv. Healthcare Mater.* **2018**, *7*, 1701164.
[30] E. B. Petcu, R. Midha, E. McColl, A. Popa-Wagner, T. V. Chirila, P. D. Dalton, *Biofabrication* **2018**, *10*, 032001.
[31] A. R. Nagle, C. D. Fay, Z. Xie, G. G. Wallace, X. Wang, M. J. Higgins, *Nanotechnology* **2019**, *30*, 195301.
[32] A. R. Nagle, C. D. Fay, G. G. Wallace, Z. Xie, X. Wang, M. J. Higgins, *Nanotechnology* **2019**, *30*, 495301.
[33] J. Gerardo-Nava, T. Fuhrmann, K. Klinkhammer, N. Seiler, J. Mey, D. Klee, M. Moller, P. D. Dalton, G. A. Brook, *Nanomedicine* **2009**, *4*, 11.
[34] Y. Wakuda, S. Nishimoto, S.-i. Suye, S. Fujita, *Sci. Rep.* **2018**, *8*, 6248.
[35] P. R. Buenzli, M. Lanaro, C. S. Wong, M. P. McLaughlin, M. C. Allenby, M. A. Woodruff, M. J. Simpson, *Acta Biomater.* **2020**, *114*, 285.
[36] C. Q. Xie, Q. Gao, P. Wang, L. Shao, H. P. Yuan, J. Z. Fu, W. Chen, Y. He, *Mater. Des.* **2019**, *181*, 108092. DOI ARTN 108092/j.matdes.2019.108092.
[37] M. Castilho, D. Feyen, M. Flandes-Iparraguirre, G. Hochleitner, J. Groll, P. A. F. Doevendans, T. Vermonden, K. Ito, J. P. G. Sluijter, J. Malda, *Adv. Healthcare Mater.* **2017**, *6*, 1700311.
[38] N. T. Nguyen, J. H. Kim, Y. H. Jeong, *Mater. Sci. Eng., C* **2019**, *103*, 109785.
[39] M. D. Ard, R. P. Bunge, M. B. Bunge, *J. Neurocytol.* **1987**, *16*, 539.